

# **Hierarchical Circuit Structure of Mouse**

## **Visual Cortex for Generating Illusory**

### **Contour Responses**



UNIVERSITEIT VAN AMSTERDAM

MSc Biomedical Sciences:  
Cognitive Neurobiology and Clinical Neurophysiology

Wouter Kroot

s13825739

July 2024

Supervisor: Prof. dr. P.H.E. Tiesinga

## Abstract

Illusory contours are edges that are perceived while no physical boundary is present. Recent studies demonstrated that mice can perceive illusory contours and identified feedback responses to be crucial for the illusory-induced activity measured in the primary visual cortex (V1). Additionally, computational work has shown that length-tuned endstopped cells can be used to delineate visual boundaries between objects, particularly when objects are partly occluded. Motivated by these findings, we propose two complementary models capable of representing the abutting grating illusion with a realistic hierarchical organisation of the mouse visual system. The first model is a Leaky Integrate and Fire (LIF) based model used to identify the requirements needed for stable endstopping. Results from the LIF model shows that when endstopped end zones are modulated by indirect inhibitory feedback mechanisms, stability is maintained when input deviates from the cell's preferred orientation. The second model, a population firing rate-based model, replicated the endstopping behaviour from the LIF-model and demonstrates how hierarchical interactions between V1 and higher visual areas can integrate endstopped cues to create perceptual boundaries that match illusory contours. These boundaries are amplified and filled in by excitatory recurrent feedback connection to V1, lifting the illusory figure from the collective organisation of inducers. Our models demonstrate how the visual cortex can fill in missing information through recurrent connectivity while also highlighting the potential of using mouse models to explore cortical organisation comparable to those in primates.

*Keywords:* Illusory contours, Endstopped cells, Primary visual cortex, Recurrent activity

# Introduction

The mammalian visual system is a complex network of interconnected areas that together process external inputs. Information enters the visual system as two-dimensional retinal activation patterns that are transformed into a coherent three-dimensional representation in the cortex. An essential part of this process is the ability to segment visual scenes into objects distinct from their background and other objects (Kirchberger et al., 2020). Early visual areas, such as the primary visual cortex (V1), perform a local analysis of visual features within relatively small receptive fields and feed their output to higher visual areas (HVAs) that integrate that information over a larger spatial extent and process increasingly abstract features. Some simple features consist of contrast and orientation, more abstract features can be shapes and ultimately encode object category (Ashbridge et al., 2000). Visual input in V1 is often clearly defined, e.g., by a luminance contrast that indicates a discontinuity such as an edge or a corner. In other cases, feedforward information can be unclear and require further processing for a robust global representation. For example, when an object is occluded by another object, the visual system must make perceptual inferences about the occluded figure and has to fill in the missing details. Interestingly, specific stimulus arrangements can induce the perception of an occluding object while no physical contour is present. Such figures are also known as illusory contours. Because the perception of illusory contours are a direct product of the underlying neural circuitry, they can effectively be used to investigate the neurophysiological interactions required

to make inferences about ambiguous or incomplete visual information.

Although many stimulus configurations make it possible to induce the perception of illusory contours, they often share common features (Palmer & Nelson, 2000). Consider the abutting grating illusion (Soriano et al., 1996) and the Kanizsa square illusion (Kanizsa, 1976). Both illusions involve extrapolations from visual cues that suggest the presence of an occluding object. In the Kanizsa square illusion, four pacman-shaped figures are arranged such that a continuous contour seems to connect the edges of the inducers. Thereby creating the illusion of a square overlapping four circles (figure 1a). Similarly, in the abutting grating illusion, the vertical alignment of horizontal lines creates the impression of a vertical contour superimposed on horizontal inducers (figure 1b). In both illusions, inducer input consists of seemingly simple geometrical forms, however, for the resulting illusion to emerge from the background inducers, they require sophisticated processing of individual inducer shapes. Namely, their position and orientation need to be processed in relation to each other. This inter-object complexity necessitates the integration of segmented stimuli, involving either hierarchical feedforward convergence or the local integration of feedback activity.

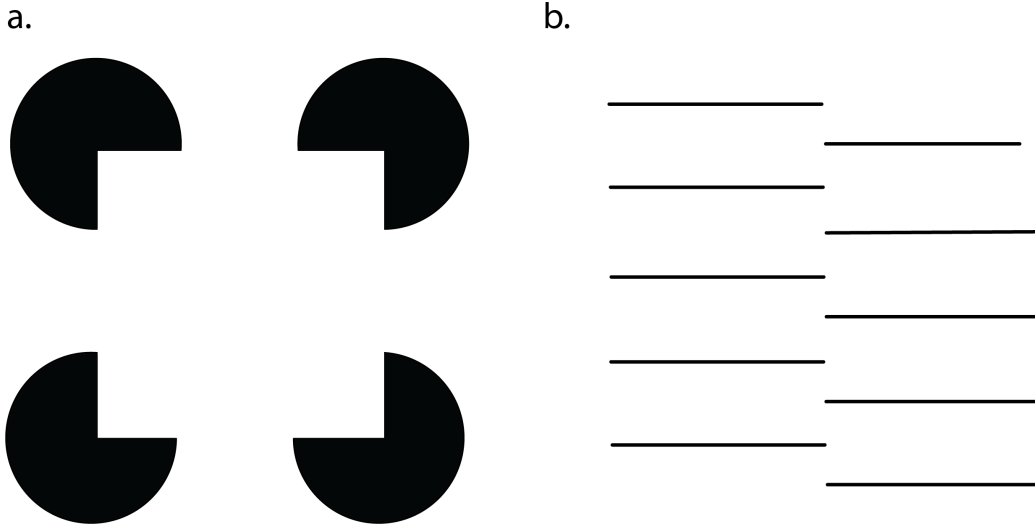


Figure 1: Illusory contour inducing figures. a. The Kanizsa illusion (Kanizsa, 1976). Four pac-man shaped inducers can be perceived as four circles with an overlapping white square. b. The Abutting grating illusion (Soriano et al., 1996). The alignment between the horizontal inducers gives the impression of a vertical contour in between the horizontal lines.

Single-unit recordings from primates have identified neurons in V1 and secondary visual area V2 (approximately 30% of cells) that react to illusory contours (Von Der Heydt & Peterhans, 1989). Interestingly, the response times in V2 precede those in V1, indicating that the first place sensitive for illusory contours in the rhesus macaque is V2 (Lee & Nguyen, 2001). A possible reason for this delay is that top-down feedback from V2 might supply the missing information about illusory contours to V1. Moreover, recurrent processing, which includes both horizontal and induced feedback connections, is involved in the perception of various illusions, suggesting that interactions between V1 and higher-order processing may be important for the generation of illusory perception (De Weerd

et al., 1996; Mendola et al., 1999; Pan et al., 2012; Roelfsema, 2006).

Recurrent activity also helps to integrate local and global visual features (Wyatte et al., 2014). This process aids in the grouping of behaviourally relevant objects and their separation from the background. By iteratively refining visual representations, recurrent processing can effectively enhance the perception of complex visual scenes (Roelfsema, 2006; Shushruth et al., 2012). This recirculation of information is associated with synaptic and conduction delays and would fit the 55 ms delay that is observed during the filling in process of illusory contours (Lee & Nguyen, 2001; Pak et al., 2020). From this perspective, illusory contours may result from a recurrent process that fills in contour information between specific inducing points that are relayed within the feedforward visual input, creating the global perception of a superimposed object. In the case that V1 illusory responses are a product of recurrent activity and real and illusory contours are processed by the same cells, a direct implication would be that higher visual areas might be unable to distinguish between real and illusory contours.

This hypothesis has been examined, identifying area V4 in macaques as a crucial integration point where both real and illusory contours are represented equivalently (Pan et al., 2012). Using optical imaging and single-cell recordings to compare neural activity elicited by real and illusory contours across area V1, V2, and V4, it was found that activity from V1 and V2 predominantly relate to the encoding of local spatial features of the inducers rather than the global orientation of the illusory contour. Meanwhile, V4 processes both real and illusory contours similarly, suggesting that hierarchical interactions govern the global orientation

processing of illusory contours.

Further support for the role of recurrent processing in the generation of illusory contours is provided by studies performed in mice. Because the extensive genetic toolkit available for mice that allows for the precise recording and stimulation of specific cells, they are exceptionally well-suited for investigating the hierarchical processing that contributes to illusory contours. Akin to the neural delays found in the macaque, mice exhibited a 30 ms delay in the representation of illusory contours compared to contours elicited by a physical contrast (Pak et al., 2020). They trained mice to differentiate between stimuli with and without illusory contours, linking their behaviour to neural activity. They showed that the representation of illusory contours in V1 was eliminated upon the silencing of LM through optogenetics, which aligns with the idea that feedback provides V1 with illusory induced activity (Wyatte et al., 2014). Although, these findings do not directly show that the generation of illusory contours is dependent on recurrent connectivity they do highlight the role of hierarchical interactions. More recent research by Shin et al. (2023) does show the importance of recurrent activity in the generation of illusory contours in mice. They found that a specific subset of V1 cells could complete the perception of an illusory contour when sufficiently stimulated. Employing decoding techniques and 2-photon stimulation, it was demonstrated that activating a particular set of V1 cells (5%) could suffice to generate the perception of illusory contours across the V1 network without any visual stimulation. These findings propose a model where recurrent feedback activity between V1 and LM underlies the generation of illusory contours in mice,

and highlight the necessity for further investigation into potential similarities and differences across species.

The visual system of mice and primates differ both anatomically and functionally. The primate visual cortex accounts for over half of their neocortex and has approximately 30 areas (figure 2a and 2b) (Felleman & Van Essen, 1991). In contrast, the mouse visual cortex includes roughly nine areas (Wang & Burkhalter, 2007). This anatomical disparity reflects the fact that mice do not primarily rely on their vision and are limited in their ability to segment figures from the background compared to primates (Luongo et al., 2023). While primates can easily segment figures using visual cues such as motion and texture, mice struggle with these tasks compared to primates. Experiments have demonstrated that mice cannot effectively use opponent motion cues for segmentation, resorting instead to brute force memorisation of specific stimulus patterns. Nevertheless, mice have shown the ability to utilise texture-based strategies for figure-ground discrimination, using patterns with different orientations and/or phases (Kirchberger et al., 2020). Both the mouse lateral medial area (LM) and the primate V2, which are implicated in the generation of illusory contours, represent the vertical meridian along their border with V1, suggesting that LM could be the homologue of primate V2 (Gămănuț & Shimaoka, 2022). The consistency between illusory contour representations in both species highlights the potential to generalise findings from mice to primates. Furthermore, primates and mice also share functional visual characteristics, such as orientation and spatial frequency selectivity (Niell & Stryker, 2008). Processing information within the cortical column follows a

hierarchical structure in mice similar to that of primates, with a clear distinction between feedforward and feedback connections. In primates, feedforward projections arise from the dorsal lateral geniculate nucleus (dLGN) and target layer 4 (L4) of V1. These feedforward signals are then transmitted from L4 to L2/3 and L5 within the cortical column. From L2/3 and L5, the feedforward signals are transmitted up into the hierarchy to L4 (Markov et al., 2014). In contrast, feedback projections originate mainly from infragranular L6 and supragranular L2/3 and target layers L1 and L6 in the lower visual stream (Rockland, 2019). The structural connectivity patterns of the cortical column of the mouse are similar to that of the primate, with the main difference being that feedforward connections are not isolated to L4 but also target supra- and infragranular layers (figure 2c). Still, feedforward information is relayed to similar cell types, predominantly targeting excitatory pyramidal cells and inhibitory parvalbumin (PV) interneurons (figure 2d). Thus, despite the smaller size and relatively lower complexity, mice have a hierarchical structure similar to that of primates. This similarity suggests that both primates and mice might process illusory contours based on the basic visual features required to represent illusory-inducing objects in lower visual areas. Therefore, to examine potential mechanical differences between mice and primates for the generation of illusory contours it is important to characterise whether orientation selective responses are a product of the feedforward convergence from the dLGN to V1 or that it is a phenomenon that emerges through cortical connectivity within V1.

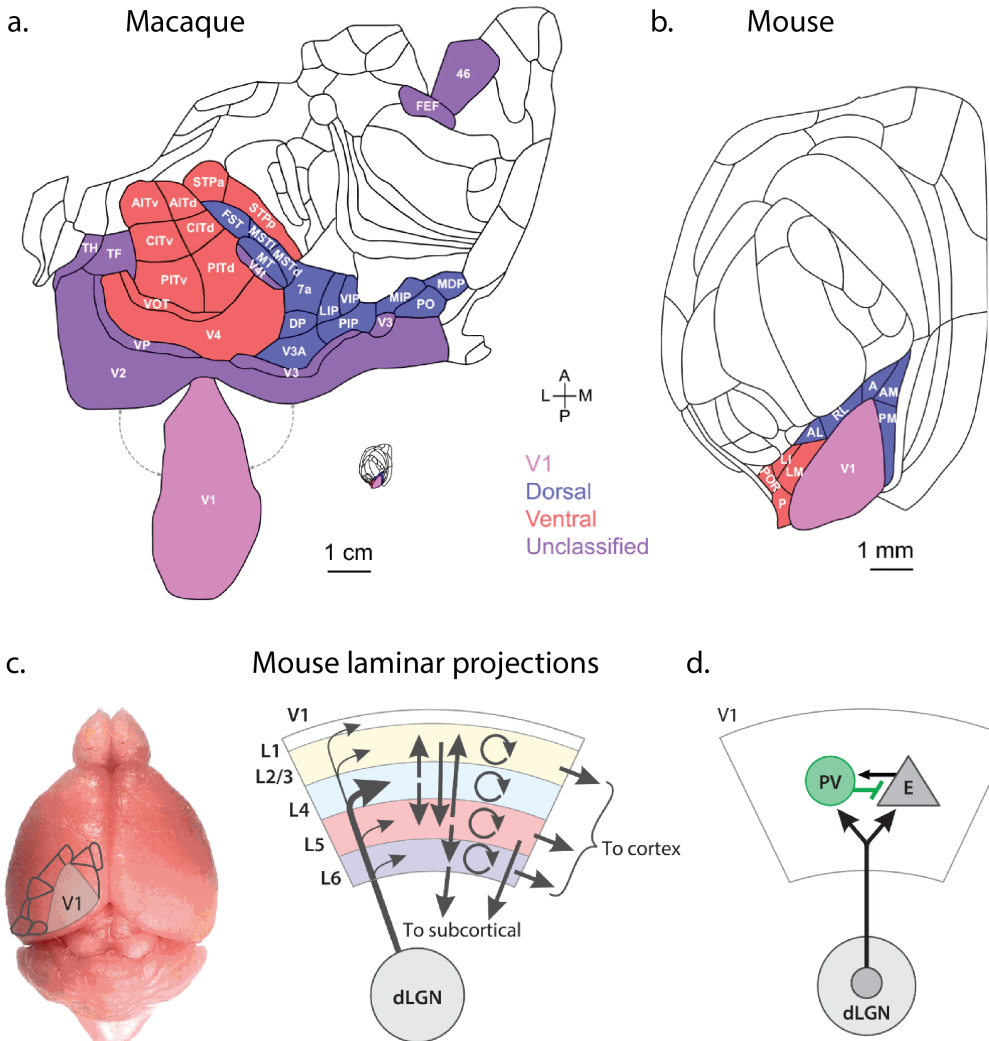


Figure 2: A comparison between the Primate and mouse visual systems. a. The macaque visual system encompasses approximately 30 areas, and therefore, is significantly larger compared to the mouse visual cortex. In the macaque, area V2 wraps around V1 as the secondary visual area. Panel a. adapted from Gămănuț and Shimaoka (2022). b. The mouse visual system, highlighting the dorsal and the ventral stream. Specifically, the ventral area LM is of importance in light of the generation of illusory contours and has been identified as a potential homologue for macaque V2. c. The visual system of the mouse mapped on a cortical image and a description of the laminar projections within V1. Laminar projections follow a similar pattern to the organisation observed in the macaque. Visual input is relayed from the dorsal lateral geniculate nucleus (dLGN) and is predominantly projected to layer 4, which in turn projects to L2/3 and L5. d. Feedforward input from dLGN to V1 mainly targets excitatory pyramidal cells and PV inhibitory interneurons, indicating that they might be important for the generation of orientation selectivity and the representation of illusion inducer objects. Panels c. and d. adapted from Niell and Scanziani (2021)

In both mice and primates the first visual cells sensitive for orientation are found in V1. Both retinal ganglion cells and their target dLGN relay cells have circularly symmetric receptive fields and respond to contrast differences within these fields. V1 neurons, however, are responsive to a number of stimulus attributes, such as orientation, motion direction, size, and binocular disparity of visual contours (Hubel & Wiesel, 1962). Early models proposed by Hubel and Wiesel (1962) emphasised the convergence of signals from the dLGN to V1, suggesting a hierarchical integration of visual information. To test whether orientation selectivity is a strict thalamocortical feedforward process or that these functional properties are a product of neuronal mechanisms on the cortical level Ferster et al. (1996) inhibited cortical spiking and measured sub-threshold responses. They found that V1 neuron orientation selectivity is largely unaffected by cortical inactivation, providing evidence that the feedforward information transmitted by the dLGN relay cells is sufficient to be transformed into orientation selective responses and that cortical circuitry is not required. Despite evidence showing similarities between mammals for how orientation selectivity originates, there are also large differences in the functional organisation across species. For instance, neurons in mouse V1 are not organised in columns with similar orientation preferences, as in primates. Mice also do not have the same pattern of functional segregation by layer that primates exhibit in which simple cells are found more in L4 and complex cells in deeper L2/3 (Martinez et al., 2005). Instead, in the mouse, simple and complex cells are evenly distributed across cortical layers (Niell & Stryker, 2008). Nevertheless, these differences in functional organisation are

demonstrated to have a minimal impact on the functional properties of orientation tuning (Hooser et al., 2005).

Physiologically, V1 neurons can be described as simple or complex cells and are both orientation selective (Skottun et al., 1991). Simple cells receive direct input from the dLGN relay cells and their receptive field responses are characterised by segregated ON and OFF fields that prefer light or dark input, respectively. These subfields are elongated taking on an elliptical shape along the axis of the neuron's preferred orientation. Due to the segregated ON and OFF subfields their responses are sensitive to changes in phase and polarity (Mechler & Ringach, 2002). In contrast, complex cells that receive input from V1 simple cells have receptive fields in which ON and OFF regions are not spatially segregated. Therefore, complex cells respond to both increases and decreases in luminance at the same location and are not sensitive to stimulus polarity or tuned to a particular phase. An important question is how the spatial offset of ON and OFF subfields are developed, since these pathways are not segregated within the LGN. Nguyen and Freeman (2019) demonstrated that through a process of Hebbian learning the ON and OFF inputs could be sufficiently segregated to produce orientation selective neurons. In their simulations they simulated a 6 x 6 degree patch of visual field and within this field randomly distributed ON and OFF channels. Then they stimulated neuronal responses using a drifting grating over the full range of orientations. Each cycle in the development process then consisted of increasing the weights of all synapses for one randomly chosen subcortical channel. If the firing rate of a cortical neuron increased as a result, the synapse between the channel and the

cortical target remained strengthened, and was otherwise decreased. After roughly 16000 cycles they found segregated ON and OFF subfields that were sufficient for orientation tuning.

This leads us into an examination of various models that attempt to explain how the visual system integrates local and global information to have a shape or contour emerge from inducer shapes. The abutting grating and Kanizsa illusions are both characterised by congruent illusory inducing points, identifiable by the presence of aligned line endings. Kanizsa inducers are considered more complex than abutting line inducers because each inducer point forms part of a corner, essentially two line ends meeting at an angle. In contrast, the abutting grating illusion is simpler, since its inducer points consist of horizontal lines. The inducer lines could be represented by individual length sensitive endstopped neurons, first classified by Hubel and Wiesel (1965) in the cat's primary visual cortex. These cells are orientation-tuned and exhibit inhibition when a line segment exceeds their excitatory receptive field into their inhibitory end zone (figure 3a). Subsequent research revealed that a significant portion of V1 simple and complex neurons exhibit endstopping to varying degrees across different species, including primates, cats, and mice (DeAngelis et al., 1994; Jones et al., 2001; Sceniak et al., 2001). Computational models expanded on these findings by demonstrating that through the integration of endstopped cells feedback responses could induce illusory neural activity. A cortical mechanism that was proposed can bee seen in figure 3b. Multiple endstopped cells are connected to a gating mechanism (X cells), which only transmits a signal when both cells are active. These

endstopped signals are then summed in a higher visual area and through feedback an orthogonal illusory response is generated (Von Der Heydt et al., 1984). The neuron in the higher visual area has been described as a bipole cell (Grossberg & Mingolla, 1987). Bipole cells are sensitive to the collinear alignment of edges in local boundary detection and are capable of integrating the output of endstopped cells to complete open boundaries. In these frameworks recurrent activity ultimately fills in the illusory contour. This type of activity is typically not present in deep neural networks (DNN). As a result, it is not surprising that feedforward DNNs fail in boundary completion tasks (Fan & Zeng, 2023).

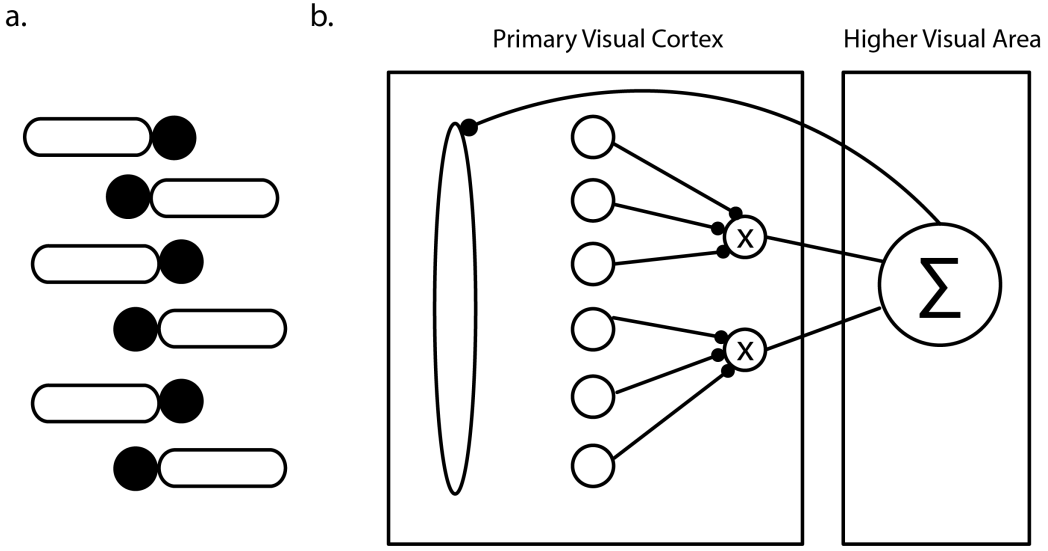


Figure 3: The proposed architecture for the representation of illusory contours in primary visual cortex. a. The receptive field characteristics of an endstopped cell. The elongated white receptive field is the excitatory zone. If a contour fitting the preferred orientation of the endstopped cell falls onto this excitatory zone, the firing rate increases. However, when the stimulus is longer and extends into the black zone of the receptive field, the firing rate is decreased. b. A proposed integration mechanism from Von Der Heydt et al. (1984). It describes how the endstopped cells can be integrated in cells that form a logic gate. When both cells are active they project a signal to higher visual area that projects feedback information to lower visual area V1. The feedback creates the V1 activation of cells that respond to the orientation of the illusory contour and not the inducer orientation.

Despite these computational insights, neurophysiological studies have largely overlooked how endstopping is integrated into higher visual areas for illusory contour perception. Previous computational simulations, while informative, have relied on feed-forward convolutions without accounting for biological constraints, such as the lack of direct inhibition observed in physiological endstopping (Sillito & Versiani, 1977) and the absence of feedback mechanisms now recognised as crucial for the representation of illusory contours in lower visual areas (Pak et al.,

2020). Addressing this gap, our current research endeavours are to (1) simulate the minimal circuit necessary for stable endstopping using leaky integrate and fire (LIF) neurons and (2) integrate endstopped microcircuits through population rate models to accurately represent the abutting grating illusion in line with physiology. Our findings identify the cell types necessary to exhibit endstopping characteristics and clarify how the orientation selectivity of pattern cells in higher visual areas modulate the representation of illusory contours through recurrent activity in V1. By incorporating endstopped cells into a hierarchical model, we aim to elucidate the neural mechanisms underlying illusory contour perception and provide a comprehensive understanding of how the visual system processes these contours across species.

## Methods

To investigate the minimal circuit necessary for endstopping and its role in generating illusory contours within the visual cortex of the mouse, the current study used two distinct computational frameworks. In the initial phase of the investigation, a LIF-based model allowed us to simulate the spatial and temporal integration of synaptic input at the single-cell level. This approach provided a foundational circuitry for orientation selectivity, complex cell features such as polarity invariance, and length-tuning. However, the current connectivity between LIF cells was set manually, and the complexity and computational demands associated with the tuning of each neuron required the current study to shift towards population models for the subsequent phase. Moreover, this phase focused on the generation of illusory contour responses through feedforward and feedback interactions. Nevertheless, the LIF network allowed us to estimate the necessary number of cells and the connectivity between them required to create a stable neural mechanism for endstopping. The population models could then abstract this behaviour into a computationally tractable form, enabling efficient simulation of illusory contour generation throughout the visual hierarchy.

To create the LIF network used for generating endstopped cells, the Brain Modelling Toolkit (BMTK) was used. We initialised an instance of the NetworkBuilder class provided by BMTK to construct an architecture of spiking point neurons, creating networks for both the dLGN and V1 separately. Then visual stimuli were presented through a three-dimensional array format ( $t$ ,  $y$ ,

$x$ ), with each entry along the first dimension (time,  $t$ ) representing a frame, and input organised along the vertical ( $y$ ) and horizontal ( $x$ ) dimensions. The BMTK simulation pipeline processed visual information through a series of steps reflecting the increase in neural complexity of the visual system. The toolkit allowed for precise control over the spatial arrangement and connectivity of neurons, facilitating the modelling of user specified neural circuits and their functional behaviours.

An important aspect of the BMTK is the segregation of the visual field as input and neural space. The BMTK has an input network called Filternet that generates firing rates from contrast present in the visual field. This effectively simulates the transformation from light intensity to neural signals as is done by the retina in visual system. Furthermore, the filter cells used in Filternet are responsive to either black or white light intensities. Thereby simulating the filtering properties of the dLGN, serving as spiking input to the cortex. This simulation environment allows for detailed analysis of how dLGN neurons process various visual inputs and contribute to the overall neural activity in V1.

V1 was simulated via a framework called Pointnet, which simulated point neuron networks within the NEST environment. NEST is well-suited for modelling point neural networks and supports the integration of predeveloped point-neuron models. This approach enabled the modelling of cortical processing of visual information, where the integration of inputs from the dLGN and the cortical circuitry results in the emergence of visual features such as orientation selectivity (Figure 4a), phase invariance (Figure 4a), and length-tuning (Figure 4c). By

separating the simulations into Filternet for the dLGN and Pointnet for the V1 cortex, we had control over the thalamocortical transformation required for orientation selectivity, and guarantee the analysis at the appropriate level of detail.

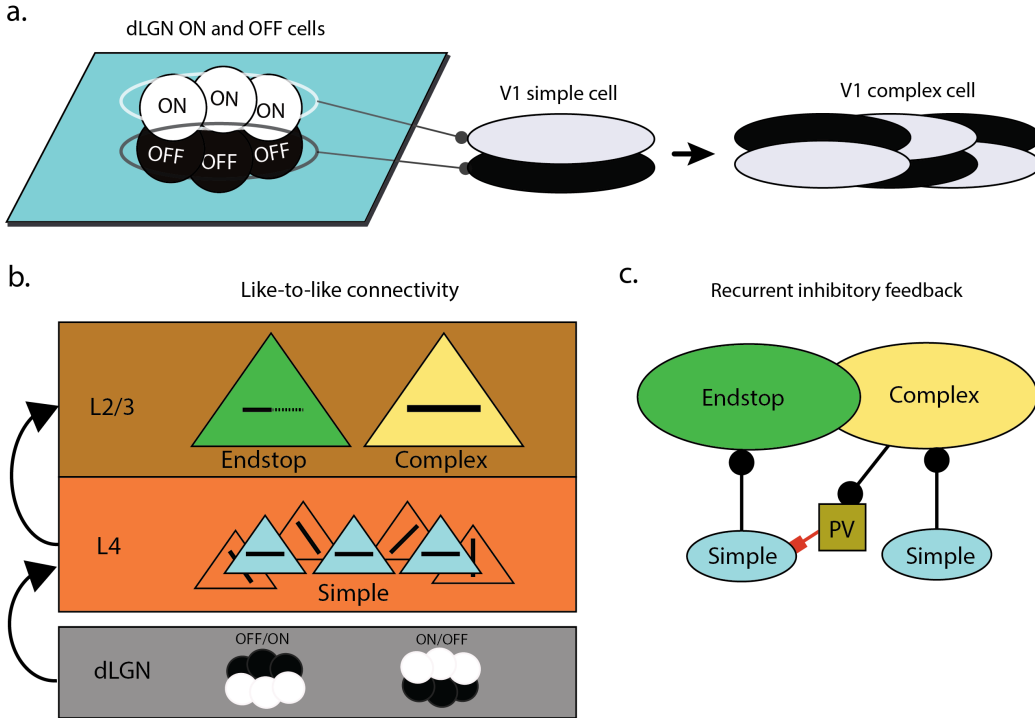


Figure 4: The generation of endstopped simple and complex cells through a recurrent inhibitory feedback microcircuit. a. The dLGN ON and OFF cells converge with a spatial offset onto a simple cell, creating a simple filter that responds to edges. Combining multiple simple cells with overlapping ON and OFF fields creates a complex cell. The complex cells, due to their overlapping subfields are not dependent on stimulus polarity and are phase invariant. b. A diagram showing the hierarchical complexity of cells that are connected based on their orientation tuning. The green endstopped cell is illustrated by a dotted line end, showing that an extended line end will result in a decreased firing rate. c. Shows how an endstopped microcircuit is made. Population of simple cells converge onto the endstopped and complex cell to give them feedforward input. However, if a line would extend over the endstopped receptive field, it will stimulate the complex cell. A recurrent inhibitory feedback loop would then inhibit the simple population that is responsible for the endstopped cell's drive and firing will decrease.

The first relay station in the visual pathway is the dLGN, which receives input from the retina and transmits visual information to V1 for further processing. The dLGN processes visual stimuli through two distinct pathways: the ON and OFF pathways, which respond to increases and decreases in light intensity, respectively. These pathways are essential for encoding contrast and edge information in visual scenes, providing the initial processing steps that shape the neural representation of visual stimuli. By presenting visual stimuli to the dLGN network, we can effectively simulate the translation of light input into neural signals, creating the first layer for contrast detection in the visual system. Since we are interested in contrast, which is encoded in V1 rather than colour, only monochromatic greyscale stimuli were shown. To transform this input array into neural signals, the dLGN was simulated as a linear-non-linear Poisson cascade model. First, visual input within the space of the receptive field of the dLGN cell is convolved with a linear filter. Then a nonlinear function is applied to the output of the previous linear filter, giving the neuron's instantaneous spike rate as its output. Finally, this firing rate generates spikes according to an inhomogeneous Poisson process (Moskovitz et al., 2018). The current dLGN model consists of two unit types, ON and OFF surround cells, optimised to closely mimic mammalian thalamic cells (Billeh et al., 2020). The ON and OFF cells of the LGN converge on a layer of simple cells, effectively exciting L4 of V1 (Figure 5a). This dual pathway of ON/OFF cells is essential for the initial segregation of visual information, setting the stage for more complex edge detection and contrast processing within higher cortical areas. We analysed spiking features in response to static images.

Therefore, we focused on modelling ON and OFF cells to have a predominantly sustained responses (sON and sOFF). We used the model templates in our node configuration to implement these cells in our network. The parameters for these cells were set based on values derived from electrophysiological recordings from the mouse dLGN, as reported by Durand et al. (2016) and Billeh et al. (2020).

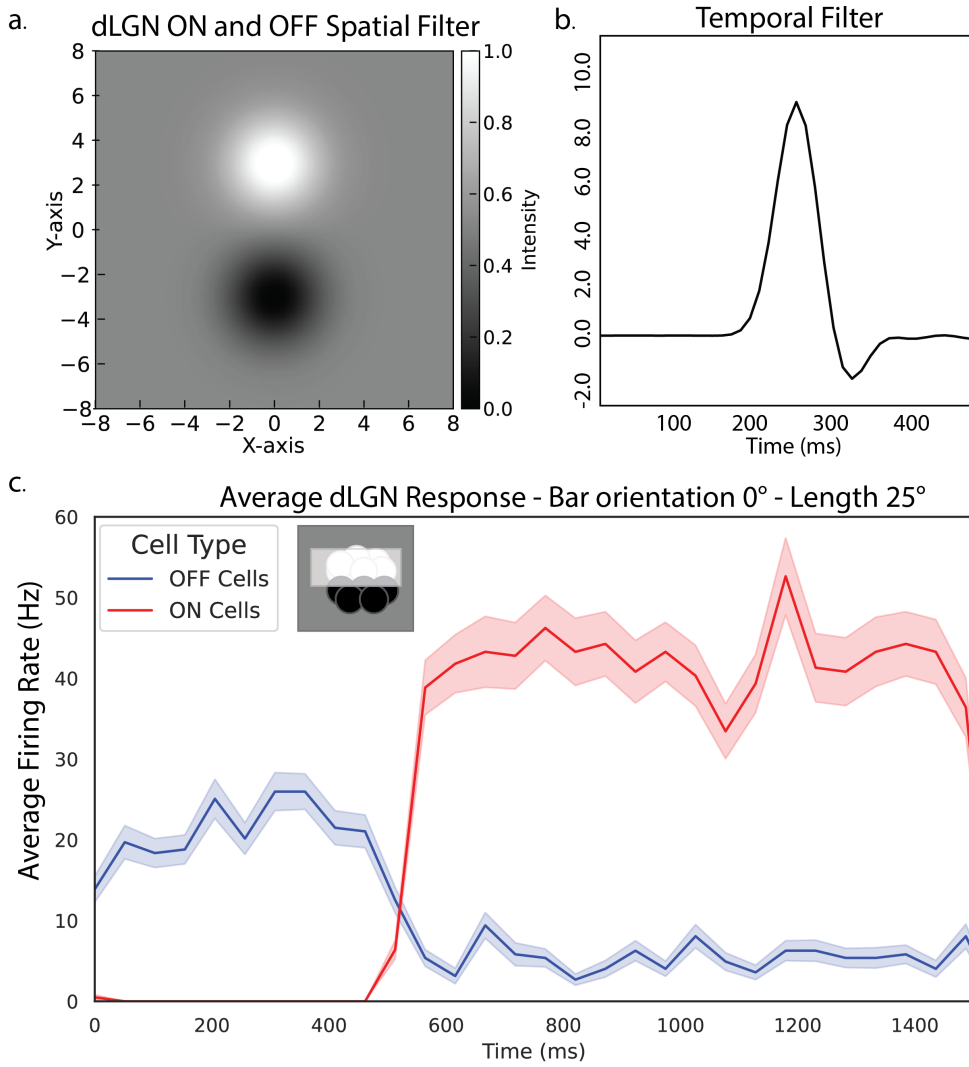


Figure 5: On and OFF cells in the dorsal lateral geniculate nucleus. a. The ON and OFF spatial filters used as input to V1 simple cells. The ON and OFF filters are two inverted Gaussian functions that are sensitive to bright and dark input, respectively. b. Each filter also has a temporal filter that dictates how the response changes through time. c. The ON and OFF response to a bar that is completely exciting the ON cells as well as some minor stimulation to the OFF cells. The stimulus is a bar with a length of 25 visual degrees and is horizontal with a rotation of 0 degrees. All stimuli presented to the dLGN were monochromatic and activated both ON or OFF cells depending on their light intensity.

For the spatial filtering of the dLGN receptive fields, we employed a Gaussian filter characterised by its spatial size and rotation. The default spatial size was set to 5.0 spatial degrees, which means the filter covered a 5-degree area in both the horizontal and vertical directions. The rotation of the filter was set to 0.0 degrees, indicating no rotation and ensuring alignment with the primary axes.

Temporal filtering was managed using a double cosine filter, which incorporates two cosine waves to model the time-dependent response of the neurons. This filter is defined by several key parameters: weights, k-peaks, and delays. The weight parameter controlled the amplitude of the two peaks in the cosine filter. The first peak had a higher amplitude (weights[0]) compared to the second peak (weights[1]). This reflects the biological observation that the initial response to a stimulus is typically stronger than subsequent responses. The k-peaks parameter determined the spread or width of the peaks. The first peak, associated with the initial response, had a narrower spread, while the second peak, representing the later response, was negative and had a broader spread. This setup ensures that the initial peak is sharp and quick, capturing rapid changes, whereas the second peak is more prolonged, capturing sustained responses.

The delay parameter controlled the timing of the peaks. The first delay (delays[0]) set the timing for the initial, larger peak, and the second delay (delays[1]) set the timing for the secondary, smaller peak. A smaller value for delays[0] resulted in a quicker initial response to changes in brightness, indicating that the neuron reacts promptly to the onset of a stimulus. Conversely, a larger value meant a slower initial response. Similarly, the value of delays[1] determined how quickly the

secondary response occurred, with smaller values indicating quicker secondary responses and larger values indicating slower ones. By carefully configuring these parameters—weights for amplitude, k-peaks for spread, and delays for timing—we ensured that the dLGN cells accurately modelled the sustained neural responses to both ON and OFF inputs necessary for our study.

Table 1: Parameters and Weights for LGN Cells

<b>Cell Type</b>	<b>Parameter</b>	<b>Description</b>
LGN	Optimised weight	(7, -1)
	Delays	(0, 0)
	K-peaks	(30, 55)

The LIF neuron model was used to represent the V1 cells. The dynamics of the membrane potential  $V(t)$  of the neuron are described by the following differential equation:

$$\tau_m \frac{dV(t)}{dt} = -(V(t) - V_{\text{rest}}) + R_m I(t), \quad (1)$$

Where  $\tau_m$  is the membrane time constant, representing the rate at which the membrane potential decays to the resting potential in the absence of input. The term  $V(t)$  is the membrane potential at time  $t$ ,  $V_{\text{rest}}$  is the resting membrane potential, which is the potential across the membrane in the absence of any synaptic input,  $R_m$  is the membrane resistance, which determines how much the membrane potential changes in response to a given synaptic current, and  $I(t)$  is the synaptic input current at time  $t$ .

The LIF model also includes a mechanism to generate spikes. When the membrane potential  $V(t)$  reaches a certain threshold  $V_{\text{th}}$ , a spike is generated, and the membrane potential is reset to a reset potential  $V_{\text{reset}}$ :

$$\text{if } V(t) \geq V_{\text{th}} \text{ then } \begin{cases} V(t) \rightarrow V_{\text{reset}}, \\ t \rightarrow t + t_{\text{ref}}, \end{cases} \quad (2)$$

where  $V_{\text{th}}$  is the threshold potential at which a spike is generated,  $V_{\text{reset}}$  is the reset potential to which the membrane potential is set after a spike, and  $t_{\text{ref}}$  is the refractory period during which the neuron is unable to fire another spike immediately after generating one. During this period, the membrane potential is held at  $V_{\text{reset}}$ .

Table 2: Parameters for V1 Cells

<b>Cell Type</b>	<b>Parameter</b>	<b>Values</b>
$V1_{\text{LIF}}$	External current	0.0 nA
	Membrane time constant	44.9 ms
	Refractory period	3.0 ms
	Resting potential	-78.0 mV
	Threshold potential	-43.0 mV
	Reset potential	-55.0 mV

To create orientation selective simple cells, dLGN were strategically connected to form elliptical receptive fields. Specifically, we designed each simple cell to have a receptive field composed of two elliptical regions: one for ON and one for OFF dLGN cells (figure 4a). These ellipses were defined by a centre position, minor axis (width), a major axis (length), and orientation angle. Each

cell had a predefined preferred orientation for identification, which was described by the angle of its major axis. Importantly, the actual preferred orientation from the cell during simulation is determined by the feedforward activity and not the cell’s identification angle. Once an dLGN cell was identified as being within the receptive field of a V1 simple cell, synaptic connections were established with specific weights and delays. These synaptic parameters were carefully tuned to reflect the physiological properties of synaptic transmission observed in biological systems, as described by Durand et al. (2016). The synaptic weights determined the strength of the input from the dLGN cell to the V1 cell, while the delays accounted for the time taken for the signal to travel between the two cells. Since the ON and OFF fields of a given simple cell are retinotopically next to each other, cells will act as an edge detector. Thus, when a drifting grating is presented to a simple cell its response will go up and down with the given pattern (figure 6a). Additionally, when the orientation of the drifting grating was changed, the cells would decrease their responses, highlighting that they are indeed orientation selective (figure 6b). These orientation selective simple cells can now be combined to create other types of cortical cells.

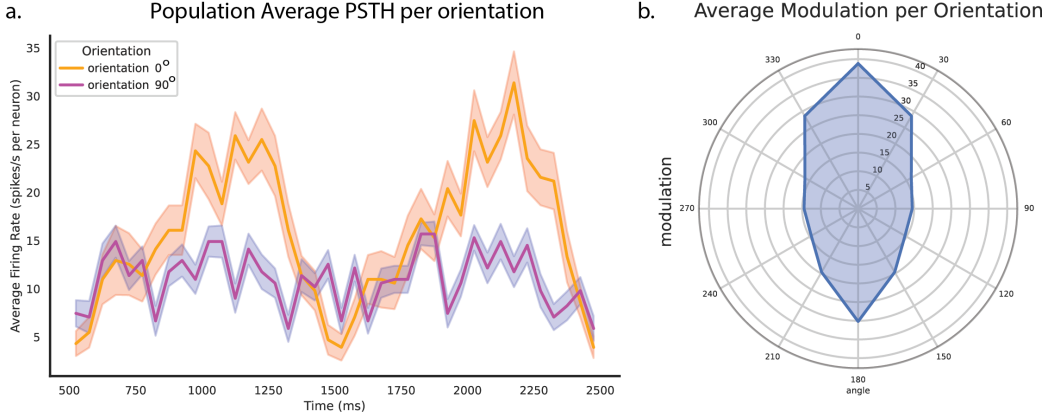


Figure 6: Orientation tuning of simple V1 cells. a. The average orientation tuning of a population of simple cells. The input was a drifting grating with different orientations. In orange the response to a horizontal drifting grating with 0 degrees orientation is shown, and in purple the response to a drifting grating with a 90 degree orientation. Simple cells show a phase sensitivity demonstrated by the two peaks, in which the cell receives no input from the dLGN. The polar plot shows the average firing modulation per orientation, showing that the cells respond to stimuli with both 0 and 180 degrees orientation.

Complex cells are characterised by their ability to respond to edges in their receptive field regardless of input polarity. To achieve this, we connected simple cells that respond to different phases of a retinotopic coordinate. We selected five ON/OFF and five OFF/ON simple cells with similar orientation preferences, resulting in overlapping ON and OFF fields (figure 4a). This overlap created a receptive field that responds to both ON and OFF feedforward inputs. The connection rule for connecting simple cells to complex cells was similar to that used for connecting dLGN cells to simple cells. It iterated over all possible simple cell sources to determine if they fell within the elliptical receptive field of the target complex cell. Because the simple cell sources had similar orientation selectivity, the resulting complex cell also followed this orientation preference.

To test whether our complex cells demonstrated polarity and phase invariance, we presented the circuit with a drifting grating in the preferred orientation of the complex cell (figure 7b). The drifting grating induced an alternating pattern between white and black in one spot of the visual field. Consequently, ON/OFF cells and OFF/ON cells showed alternating peaks in activity, while complex cells maintained a stable firing pattern. In figure (figure 7a), the simple cell types clearly showed peaks at 30 Hz, decreasing to 0 Hz. In contrast, due to the converging simple cells, the complex cells exhibited stable activity above 30 Hz, as highlighted in the raster plots (figure 7c). With these fundamental cell types and the addition of inhibitory interneurons, it is possible to create endstopped length-tuned cells.

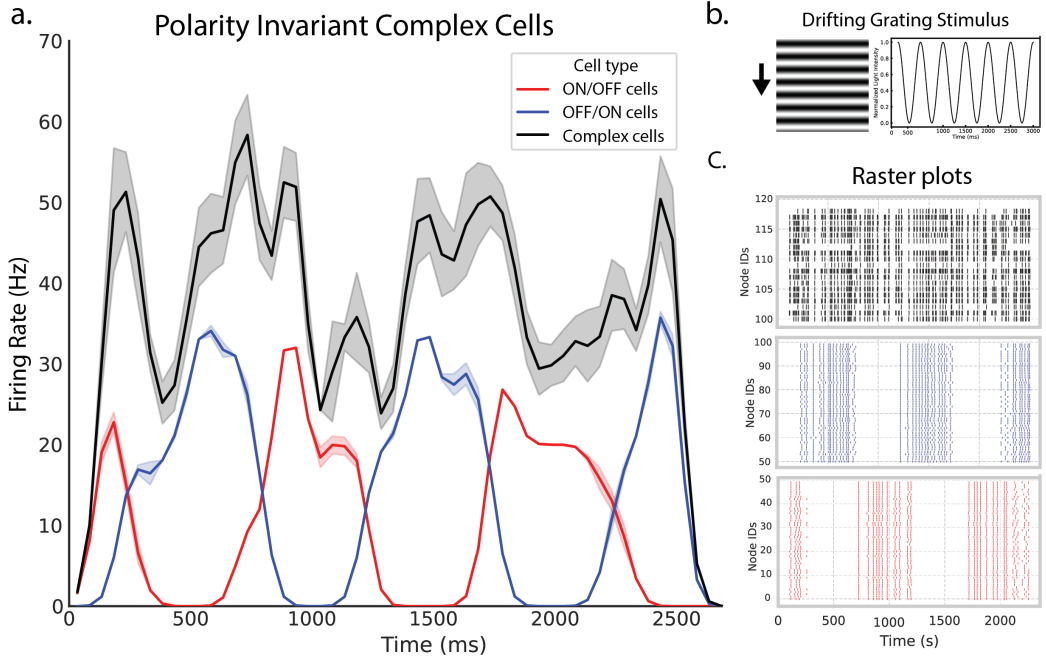


Figure 7: Simple and complex cells responses to a horizontal drifting grating. a. ON/OFF simple cells are shown in red with an offset phase from the OFF/ON cells. The black complex cells do not exhibit the same phase sensitivity but have a more stable response to the ON and OFF alternating stimulus contrast. b. The drifting grating stimulus that was presented to the model. The orientation of the drifting grating matched the preferred orientation of all cell types. c. The raster plots also illustrate the phase sensitivity of the simple cells and how the complex cell has a stable firing to a constantly fluctuating input.

One goal of the model was to experiment with generating stable endstopping using dLGN, simple, and complex cell types. Initially, an attempt was made to create endstopping by combining spatially offset simple cells in a strictly excitatory manner, modelling the inhibitory subfield with an OFF field and the excitatory subfield with an ON field. While this method reduced the firing rate, it did not achieve a zero spiking rate for long inputs due to the excitatory nature, which could only lose half the input based on polarity. To address this, we decided to

include a recurrent inhibitory loop from a laterally displaced complex cell to a neighbouring simple cell population. The displacement introduced a spatial offset between the excitation source and the inhibitory location. Resulting in a feedback loop that suppresses cell activity when a stimulus extended beyond their receptive field, the main characteristic of an endstopped cell. Because the inhibitory cells are targeted by a complex cell, the decrease in firing rate is contrast insensitive (figure 4c). The weights that were used to connect each cell type are presented in table 3.

Table 3: Connection Weights in the LIF endstop Circuit

<b>From</b>	<b>To</b>	<b>Weight</b>	<b>Delay (ms)</b>
dLGN (e)	Simple (e)	0.8	0.2
Simple (e)	Endstopped (e)	0.8	0.2
Simple (e)	Complex (e)	0.7	0.2
Complex (e)	PV (i)	2.5	0.2
PV (i)	Simple (e)	-3.0	0.2

To investigate how endstopped cells can be effectively integrated into higher visual areas, we used neural population models instead of LIF cells while maintaining the same neural architecture. These population models allowed us to recreate interlaminar connections by treating each functional cell type as a population, enabling us to study how they collectively encoded the presence of illusory contours. This abstraction facilitated the addition of a higher visual cortical area, LM, which integrated V1 endstopped responses and provided cell-type-specific recurrent feedback.

The cells that integrated the endstopped responses are called pattern cells, created

based on the feedforward orientation selectivity of the endstopped sources. Their feedback targeted orthogonally tuned complex cells, corresponding to the orientation of the resulting illusory contour (figure 8). This way, specific endstopped cells were active due to the horizontal inducers, without activating the inhibitory feedback loop. If enough inducers were active, those signals would be integrated and activate the LM pattern cells, resulting in an excitatory feedback loop that fills in the illusory contour between the inducers.

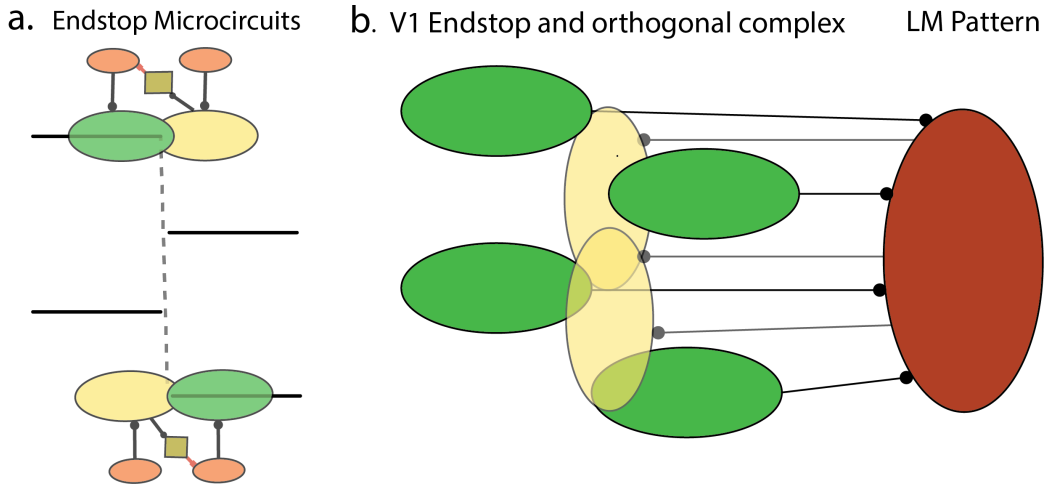


Figure 8: The architecture used to represent illusion inducer objects through the feed-forward endstopped signals and the representation of illusory contours through feedback responses. a. The endstopped microcircuit illustrated on top of horizontal abutting grating illusion inducers. The cells are colour coded following (figure 4). b. If all 4 of the endstopped cells are active they fire enough to activate a higher visual pattern cell in LM, which integrates these input and projects feedback onto orthogonally tuned complex cells. This way an illusory contour is locally represented through the integration of local endstopped signals.

The population mass model we used was the Wilson and Cowan model (Wilson & Cowan, 1972). The model describes the dynamics of excitatory and inhibitory neural populations through coupled differential equations. The rate equations for the excitatory and inhibitory populations are given by:

$$\begin{aligned}\tau_e \dot{r}_e &= -r_e + (k_e - q_e r_e)S(c_{ee}r_e + c_{ei}r_i + I_e(t)), \\ \tau_i \dot{r}_i &= -r_i + (k_i - q_i r_i)S(c_{ie}r_e + c_{ii}r_i + I_i(t)),\end{aligned}$$

where  $\tau_e$  and  $\tau_i$  are time constants for the excitatory and inhibitory populations, respectively, and  $r_e$  and  $r_i$  are the firing rates of these populations. The constants  $k_e$ ,  $k_i$ ,  $q_e$ , and  $q_i$  relate to the maximum firing rates and their saturation. The coupling coefficients  $c_{ee}$ ,  $c_{ei}$ ,  $c_{ie}$ , and  $c_{ii}$  represent the connection strengths between the populations, while  $I_e(t)$  and  $I_i(t)$  are the external inputs to the excitatory and inhibitory populations, respectively.

The sigmoid function  $S$ , which transforms the combined synaptic inputs into a firing rate, is given by:

$$\text{sigmoid}(x) = \frac{1}{1 + e^{-x}}$$

In the context of the Wilson-Cowan model, the sigmoid operation is expressed as:

$$m = \text{sigmoid}(s \cdot (r_{\text{exc}} + r_{\text{inh}} - \theta)) - \text{sigmoid}(-s \cdot \theta)$$

Here,  $r_{\text{inh}}$  represents the inhibitory input, and  $r_{\text{exc}}$  represents excitatory inputs. The parameters  $s$  and  $\theta$  control the slope and threshold of the sigmoid function,

respectively. The sigmoid function normalises the input, producing an output firing rate  $m$  that captures the balance between excitatory and inhibitory inputs. This transformed firing rate is then used in the rate equations to describe the dynamic behaviour of the neural populations.

The range of the firing rate  $r$  is determined by the steady-state solutions of the rate equations. Given the typical parameters and the properties of the sigmoid function, which ranges between 0 and 1, the firing rate  $r$  will also range between 0 and a maximum value that depends on the specific parameters of the model. For the given parameter values (see Table 4), the firing rate  $r$  is expected to range approximately from 0 to 0.5. The model output is then multiplied by 100 to represent the firing rate in spikes per second, resulting in a range from 0 to 50 spikes per second (Hz). This range captures the steady-state behaviour under typical neural conditions and the balance of excitatory and inhibitory inputs.

To model neural populations, we used node templates. The excitatory population node template combines the rate operator and the synaptic excitation operator to represent a group of excitatory neurons, which promote activity in the network. Conversely, the inhibitory population node template combines the rate operator and the synaptic inhibition operator to represent a group of inhibitory neurons, which suppress activity in the network. These node templates can be combined to form a circuit template defining the overall network structure of the model. The parameters used in the model are summarised in Table 4.

Table 4: Parameters of the Wilson-Cowan Neural Mass Model

Parameter	Description	Value
$s$	Steepness of the sigmoid curve (excitation)	1.0
$\theta$	Threshold for excitation	2.0
$r_{\text{inh}}$	Inhibitory state of the population	0.0
$r_{\text{exc}}$	Excitatory state of the population	0.0
$s$ (inhibition)	Steepness of the sigmoid curve (inhibition)	2.0
$\theta$ (inhibition)	Threshold for inhibition	2.5
$k$	Coupling term	1.0
$\tau$	Time constant (ms)	10.0

The connections between these nodes are specified with weights that determine the strength and type of influence they exert on each other. The weights for these connections are as follows: the rate output  $r$  of the Simple node feeds into the synaptic excitation input  $r_{\text{exc}}$  of the Endstop node with a weight of 7.0, the rate output  $r$  of the Simple node also feeds into the synaptic excitation input  $r_{\text{exc}}$  of the Complex node with a weight of 7.0, the rate output  $r$  of the Complex node influences the PV node's synaptic inhibition input  $r_{\text{inh}}$  with a weight of 7.0, the rate output  $r$  of the PV node reduces activity in the Simple node by feeding into its synaptic inhibitory input  $r_{\text{inh}}$  with a weight of -14.0, and the rate output  $r$  of the pattern node feeds into the synaptic excitation input  $r_{\text{exc}}$  of the Complex (e) node with a weight of 12.0. The specifications of these weights are outlined in Table 5.

Table 5: Connection Weights in the Wilson-Cowan Circuit

<b>From</b>	<b>To</b>	<b>Weight</b>
Simple (e)	Endstop (e)	7.0
Simple (e)	Complex (e)	7.0
Complex	PV (i)	7.0
PV (i)	Simple (e)	-14.0
Pattern (e)	Complex (e)	12.0

## Data analysis

All data analyses and visualisations were performed using the Python programming language (Van Rossum & Drake Jr, 1995). First, spiking data was structured with a spike timestamp and a cell identification number. To track the specific cell types each cell also had a complexity identification number, corresponding to simple, complex or endstopped cells. This way each cell could be identified post simulation. The identification number only served as a way to retrieve the spikes of a particular set of cells. To visualise and analyse the spike trains over time, peristimulus time histograms (PSTH) were used. To create the PSTH, elicited spikes were counted over multiple cells per time bin (50 ms). In order to quantify the firing rate as a temporal average, the firing rate ( $v_c$ ) in cell  $c$  is the spike count ( $n_{sp}^c$ ) in an interval of duration  $T$  divided by  $T$ .

$$V_c = \frac{n_{sp}^c}{T}$$

To visualise the average response of multiple neurons the cells were averaged per time bin. The resulting signal was then smoothed by convoluting the averaged

PSTH with a Gaussian kernel to make trends in the data more pronounced. Additionally, the y-axis limits were fixed based on the largest response in the test.

In order to preserve single cell dynamics, the PSTH of the evoked responses of individual cells were used to calculate the modulation and endstopping accuracy. The modulation is defined as the difference between the maximum and minimum non-zero firing rates.

$$\text{Modulation} = \max(\text{FR}_{\text{non-zero}}) - \min(\text{FR}_{\text{non-zero}})$$

Where  $\text{FR}_{\text{non-zero}}$  represents the non-zero firing rates.

To calculate the Signal-to-Noise Ratio (SNR), we convert the PSTH data to firing rates (in Hz) and smooth the data using a Gaussian filter. We then fit a quadratic polynomial to the smoothed firing rate data within a specified analysis window. The SNR is quantified by calculating the penalised R-squared value, which accounts for any firing rates that exceed a threshold after a specified penalty time. The formula for the penalised R-squared value is:

$$R^2_{\text{penalised}} = \left(1 - \frac{SS_{\text{res}}}{SS_{\text{tot}}}\right) \times P$$

Where  $SS_{\text{res}}$  is the residual sum of squares,  $SS_{\text{tot}}$  is the total sum of squares, and  $P$  is a penalty factor that reduces the R-squared value if the firing rate exceeds a 20 Hz after the endstopped time window. We conducted an analysis to compare the endstopped accuracy measurements across the different network configurations.

To assess the normality of the SNR value distributions, we employed the Kolmogorov-Smirnov (K-S) test and generated quantile-quantile (Q-Q) plots. Given that the SNR values did not follow a normal distribution, we used the Mann-Whitney U test for pairwise comparisons between the networks. This non-parametric test is suitable for comparing distributions of two independent samples with unequal sample sizes. Pairwise Mann-Whitney U tests were conducted for all combinations of network configurations, calculating the test statistic and p-value for each comparison, results were adjusted for multiple comparison using the false discovery rate (FDR) with an alpha of 0.05.

## Results

To investigate the role of recurrent inhibition in the process of endstopping, we developed a LIF-based point neuron model using a microcircuit architecture of simple, complex, and inhibitory interneurons. The simple cell population at a specified retinotopic coordinate connects to a complex cell. The complex cell in turn connects to a number of PV cells, creating an inhibitory feedback loop that suppresses the activity of a neighbouring simple cell population. This configuration allows us to simulate the behaviour of endstopped cells in response to line segments of varying lengths and orientations. Then we also presented bars that continuously increased in size to gain insights into the stability of endstopping over time. Additionally, to determine the optimal cell type ratio and the minimal number of endstopped cells required for stable responses, we systematically varied cell type quantities and observed the resulting responses. The LIF architecture was then recreated in a population-based neural model, which we used to present stimulus configurations that were empirically observed to either elicit or disrupt the perception of the abutting grating illusion (Von Der Heydt & Peterhans, 1989).

The endstopping responses elicited by static bars are illustrated in figure 9. The four subplots show the average firing rates of neurons presented with bars of lengths: 5, 10, 15, and 20 visual degrees at four orientations:  $0^\circ$ ,  $15^\circ$ ,  $30^\circ$ , and  $45^\circ$ . At  $0^\circ$  orientation, the firing rates display the responses to the preferred orientation of the endstopped cells (figure 9a). The bar of length 10 elicits the

highest response because only the excitatory component of the endstop-circuit was stimulated. The firing rates peak at 70 Hz between 100 and 200 ms after stimulus presentation, showing a sustained response beyond 1000 ms. As bar length increases, peak firing rates decrease, inhibiting the sustained response. Next, when the orientation of the presented bar increases, we observed a gradual decline in the elicited firing rates. At a  $15^\circ$  orientation, the response pattern shifts slightly. The 15 visual degree bar still evokes the highest firing rate, but the peak is slightly lower than for  $0^\circ$  orientation, at around 50 Hz (figure 9b). Moreover, the relative difference between the elicited responses between the 10 and 15 visual degrees bars are smaller compared to the horizontally oriented bar at  $0^\circ$  orientation. This trend continues as the bar is further rotated as can be seen in figure 9c. In figure 9d, the extended bar does not reach the receptive field of the complex cell, resulting in no relative differences between bar-lengths and the absence of endstopping.

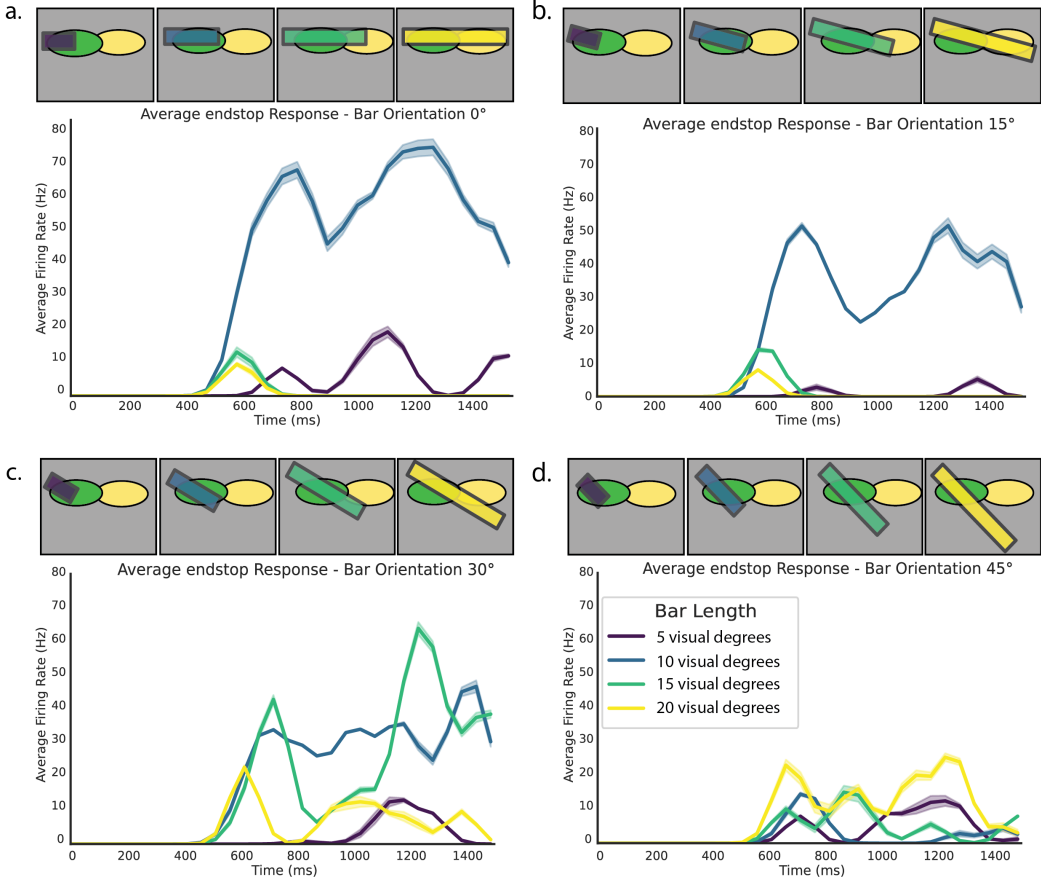


Figure 9: Neural responses of the endstopped complex cells to line segments with different lengths: 5, 10, 15, 20 visual degrees, and orientations  $0^\circ$ ,  $15^\circ$ ,  $30^\circ$ ,  $45^\circ$ . a. The optimal endstopped response to a line with orientation  $0^\circ$ . A large difference in peak activity between length 10 and 20 visual degrees. The x-axis represents the simulation time, and the y-axis represents the firing rate of the complex cell in spikes per second (Hz). The cell types are colour coded according to stimulus length, and presented in the legend of panel d. b. The relative difference decreases when the line segment is rotated away from the preferred orientation. c. Endstopping decreases further and responses are more similar to complex cells. d. Endstopping is completely decreased as the line segment does not activate the inhibitory inducing end zone.

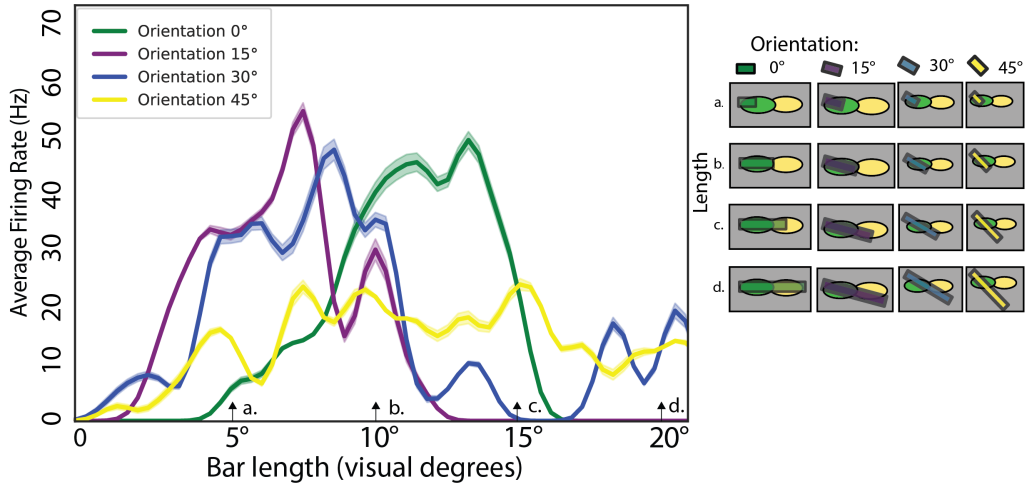
To gain a better understanding of the subtle differences related to the bar length over time, we stimulated the model with a continuously growing bar. Again,

we also varied the orientation of the growing bar, as shown in figure 10a. The bar start at the beginning of the excitatory receptive field and gradually extends into the endstopped inhibitory end zone. The line plot on the left shows the average firing rate (Hz) of the endstopped cells as a function of bar length in visual degrees, with the shaded area representing the variability around the mean. For the cell's preferred orientation ( $0^\circ$ ), the average firing rate increases steadily, peaking at 50 Hz. This peak indicates the optimal bar length that maximally activates the excitatory zone of the endstopped neurons. Beyond this length, the firing rate declines, reflecting the inhibitory effect as the bar extends into the adjacent complex cell's receptive field. Because the width of the stimulus bar slightly extended over the endstopped receptive field we observed an increased shift in the response when the bar's orientation was increased. However, the maximum firing rate of 50 Hz was maintained across orientations  $15^\circ$  and  $30^\circ$ . When qualitatively comparing the response shapes across the different orientations we observe that the response to the preferred stimulus orientation has a rounder shape than the other orientations. Indicating that the preferred orientation is represented best compared to the other stimuli.

Importantly, figure 10b allows for the comparison between our findings and the endstopped responses of a hypercomplex cell from cat V1 (Orban et al., 1979). Because mice have smaller receptive field sizes compared to cats the stimulus lengths are different. This figure shows that our endstopped cells have similar response shapes as actual endstopped cells. In contrast, a key difference is that the modelled cells show similar peak firing rates to the different orientations,

which the physiological endstopped cells did not. Notably, previously described endstopped responses to static bars did show the gradual decrease when deviating from the cell's preferred orientation (figure 9). Another difference is that our simulated endstopped cells show a steeper decline when the bar extends into the inhibitory end zone compared to the gradual decline found in the cat endstopped cell.

a. Endstopping response to a continuously growing bar



b. Hypercomplex cell cat V1

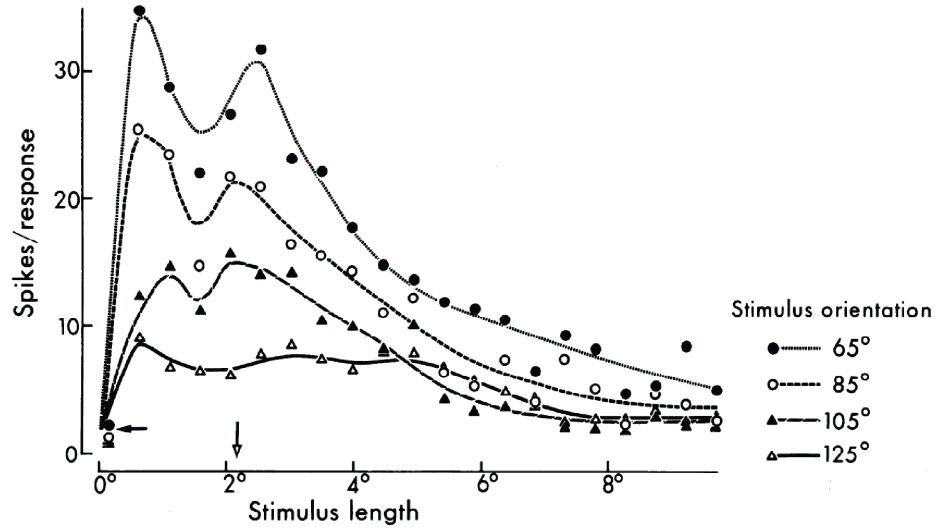


Figure 10: The responses of an endstopping population stimulated with a continuously growing bar. a. The population has a preferred orientation of 0°. The response to the 0° bar segment shows that the firing rate slowly ramps up to a maximum of 50 Hz, to the line being around 12 visual degrees in length, after which firing rate is quickly decreased for longer inputs. Bar stimuli that deviate from the preferred orientation show similar peak firing rates, but show a less rounded peak response compared to the 0° degree bar. b. The endstopped response of a physical hypercomplex cell in cat V1. The receptive field sizes of cat V1 hypercomplex are smaller than that found in the mouse. Panel b. was taken from Orban et al. (1979).

To further quantify the endstopping mechanism influenced by different cell types, we analysed the average endstopping responses of networks with varying compositions of endstopped cells. We investigated networks with 1, 5, 10, 20, and 40 endstopped cells while adjusting the ratios of simple cells to PV cells to observe the resulting endstopping responses. Specifically, Network 1 included 1 endstopped cell, 1 complex cell, 20 simple cells, and 10 PV interneurons (1:2). In Network 5, the composition was adjusted to 5 endstopped cells, 5 complex cells, 50 simple cells, and 10 PV interneurons (1:5). Network 10 featured a balanced mix of 10 endstopped cells, 10 complex cells, 100 simple cells, and 20 PV interneurons (1:5). Network 20, which demonstrated the highest endstopping accuracy, consisted of 20 endstopped cells, 20 complex cells, 500 simple cells, and 50 PV interneurons (1:10). Finally, Network 40 was composed of 40 endstopped cells, 40 complex cells, 1000 simple cells, and 50 PV interneurons (1:20).

The Mann-Whitney U test results revealed significant differences in SNR values between several network configurations, with Network 20 showing particularly notable differences. Specifically, comparisons between Network 20 and other networks indicated significant differences: Network 1 vs. Network 20 ( $U = 0.0$ ,  $p = .026$ ), Network 5 vs. Network 20 ( $U = 0.0$ ,  $p < .001$ ), Network 10 vs. Network 20 ( $U = 0.0$ ,  $p < .001$ ), and Network 20 vs. Network 40 ( $U = 800.0$ ,  $p < .001$ ). These results suggest that the SNR values in Network 20 are distinctly different from those in Networks 1, 5, 10, and 40. Among these configurations, Network 20 achieved the highest endstopping accuracy, with an  $r^2$  value of 0.67, maintaining a PV to simple cell ratio of 1:10, indicating the optimal balance

between PV and simple cells for endstopping accuracy in our LIF model.

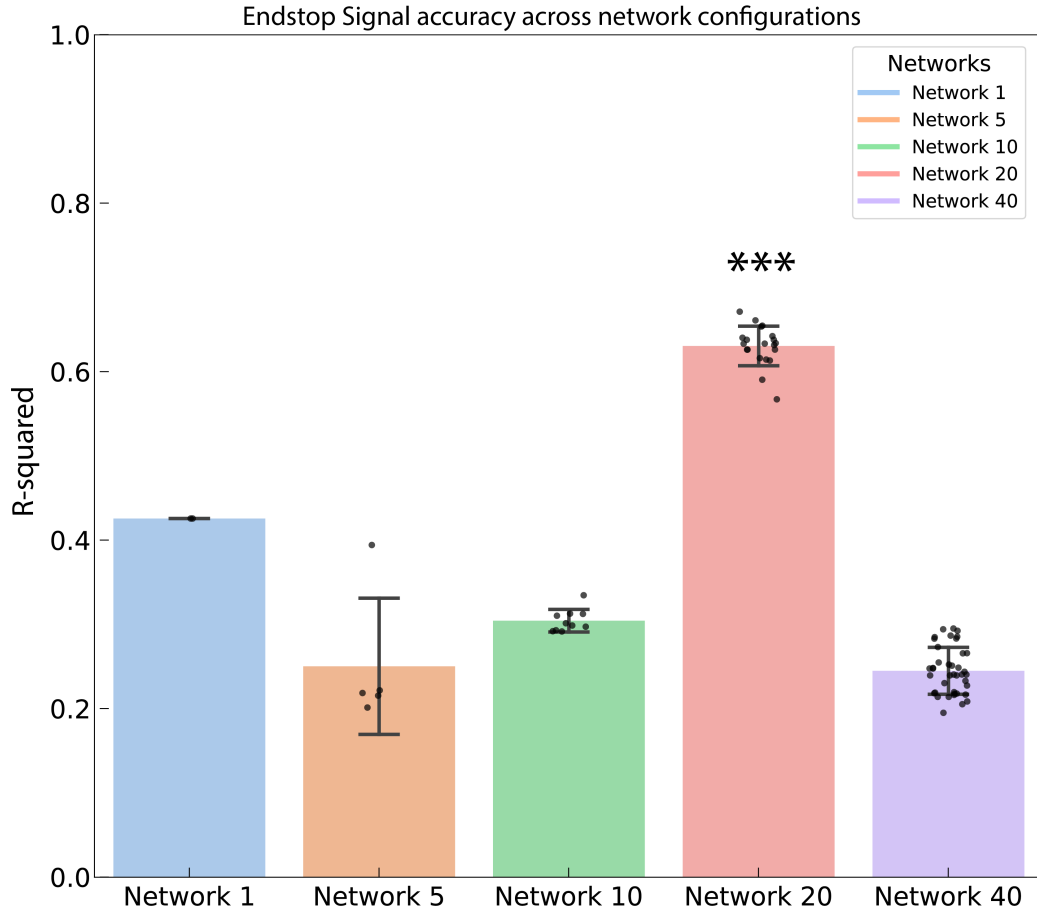


Figure 11: The average endstopping responses of networks with 1, 5, 10, 20, and 40 endstopped cells were analysed. Endstopping accuracy was quantified by fitting a quadratic polynomial to the smoothed PSTH response to a bar continuously increasing in length along the cell's preferred orientation. The network with 20 endstopped cells exhibited the highest endstopping accuracy, with a PV to simple cell ratio of 1:10,  $r^2 = 0.67$ . \*\*\* indicated  $p < 0.001$ .

Next, we examined whether our population model reflected results found during physiological experiments done with the abutting grating illusion (Von Der Heydt & Peterhans, 1989). They showed that the illusory contour breaks down when a

horizontal gap is introduced that misalign the horizontal inducers. Additionally, they demonstrated that when a bar crosses the illusory line illusory responses decreased as well. Figure 12 showcases the responses of different cell types to visual stimuli designed to induce the perception of illusory contours. The left panels of each sub-figure (a, b, and c) display the mean firing rates of complex cells tuned to 90 degrees for the illusory response, complex cells tuned to 0 degrees that are tuned for the inducer lines and to create endstopped circuits. Also, the responses of pattern cells are shown, which integrate signals from the endstopped cells and project back to the 90 degree complex cells. The right panels depict the spatial arrangement and the type of stimulus presented, as previously described. The colour coding indicates the average firing rates, with warmer colours representing higher activity levels. The complex cells (dotted outlines) and end-stop cells (solid outlines) are shown in their spatial positions, providing a visual representation between cell type, location, and stimulus-induced activity.

In subfigure (a), the stimulus created a strong illusion because inducers were horizontally matching the orientation preference of complex 0° endstopped cells and were vertically aligned, so the pattern cell was maximally stimulated. The robust mean firing rate of the complex 90° cells, peaking around 40 Hz, suggested effective encoding of the perceived illusory contours. When the stimulus is modified in sub-figures (b) and (c) to disrupt the illusion, the complex 90° cells' activity changes significantly. Sub-figure (b) shows a disruption of the illusion due to a horizontal inducer crossing the illusory contour, reflected by a reduced

firing rate of the complex cells. Still, the response off the complex  $90^\circ$  remained around baseline (8 Hz), indicating a potential for illusory contour but not enough to effectively activate the pattern cell population. In sub-figure (c), the stimulus is further modified, introducing a horizontal gap between inducers to break the illusion. The firing rate of the complex  $90^\circ$  cells drops significantly compared to sub-figures (a) and (b). This substantial reduction in activity indicates that the stimulus no longer supports the perception of the illusory a contour.

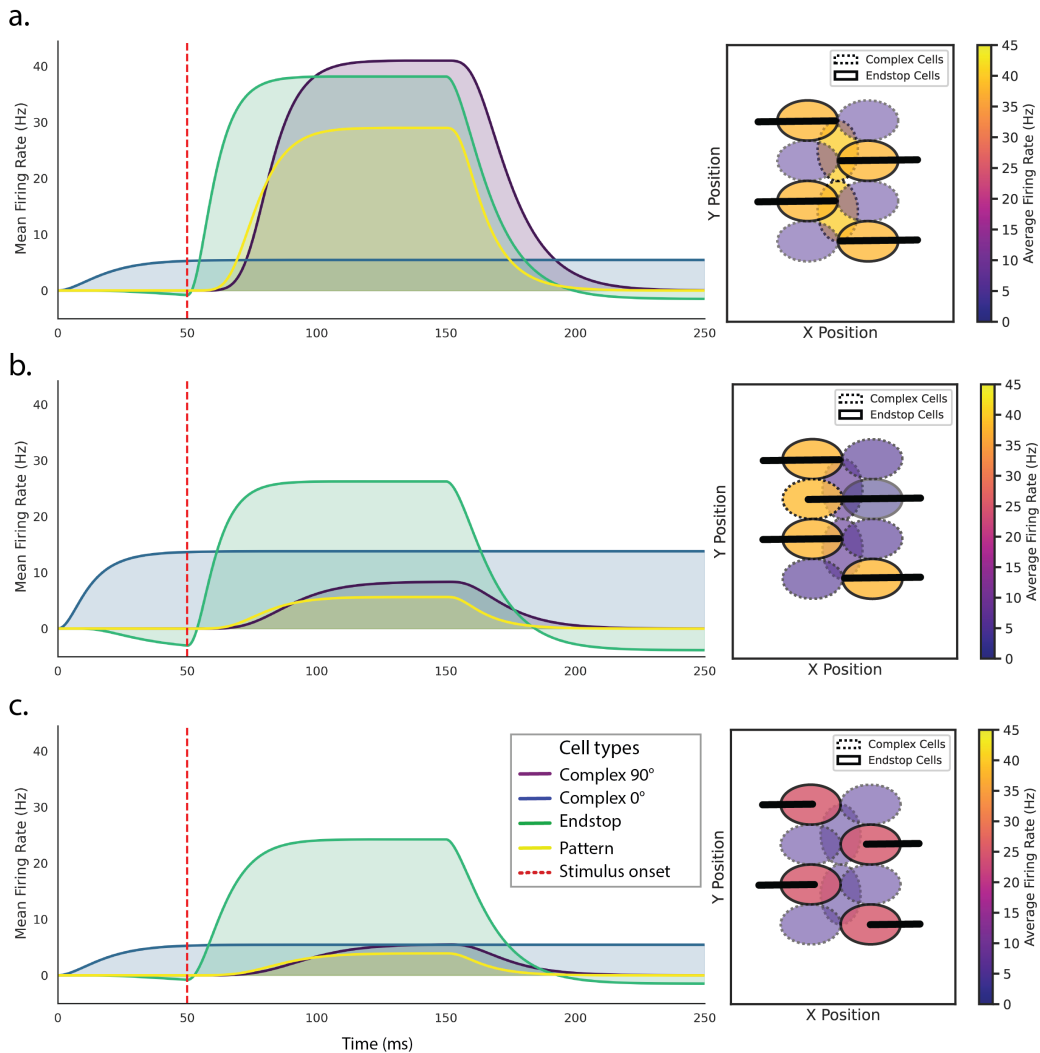


Figure 12: Population responses to the abutting grating illusion. a. The optimal input is given to the model, all inducers are the preferred orientation and are spatially aligned. All endstopped populations are very active, and the complex end zones are not active, thus resulting in maximum representation of the illusory contour. b. In this example one of the inducers crosses the illusory contour, resulting in the abolishment of the illusion. The complex end zones increase in activity and thus the activity of the endstopped cell also decreased, and no illusory contour is formed. c. Similarly, in this figure the inducer lines are not aligned enough to form a strong illusory contour. The complex end zones are not activated, but also the endstopped cells are not maximally stimulated. Therefore, the pattern cell is not stimulated, and no illusory contour is formed.

## Discussion

In the current study, we demonstrated that endstopping can be generated through recurrent inhibitory connectivity and can be integrated by a higher visual area to drive excitatory recurrent contour completion. We modelled endstopped cells by creating a LIF-microcircuit of two adjacent populations of complex cells that were connected through an inhibitory feedback loop to the respective simple cells. This setup produced length-tuned endstopped cells that reduced their firing rate when a stimulus edge extended beyond the excitatory receptive field into the inhibitory end zone. The LIF-model demonstrated that endstopped cells are a suitable neural mechanism for detecting the line ends that induce the abutting grating illusion. To illustrate the representation of the abutting grating illusion using endstopped signals, we implemented a second model with population firing rate equations. The abstraction from point neurons to neural populations ensured a stable firing rate without the need for extensive weight tuning between individual cells, allowing for the extension of the LIF-model architecture with a higher visual area, LM. Results from the population model demonstrated that LM pattern cells are able to group retinotopically aligned endstopped cells and generate the illusory activity in V1 through recurrent excitatory connections. These models complement each other and demonstrate the importance of recurrent inhibitory and recurrent excitatory activity for filling in missing information in V1.

Central to our endstopping simulations is that we used recurrent inhibitory

connections to induce the inhibitory end zones. The use of recurrent inhibition is in line with the observations that inhibitory influences are not exerted directly on endstopped cells (Sillito & Versiani, 1977). Our results suggest that the segregation of inhibition can serve a functional physiological purpose. Namely, PV interneurons have been found to adaptively modulate excitatory signals based on the visual context. When input is present outside a cell’s feedforward generated receptive field, their response can still be modulated through horizontal and feedback activity (Schnabel et al., 2018). By measuring visual responses and synaptic connectivity of PV cells and pyramidal cells it was observed that PV and pyramidal cells share visual selectivity (Znamenskiy et al., 2024). Due to recurrent inhibitory activity between pyramidal and PV cells, PV cells were shown to actively stabilise excitatory activity within feature-specific ensembles while supporting competition between pyramidal cells. As a result the broad tuning of inhibitory cells provide a cortical mechanism to sharpen the tuning of pyramidal cells by reducing membrane potential responses to non-preferred stimuli (Li et al., 2012). As shown in figure 10, endstopped responses in our model also show sharper response shapes to preferred orientations compared to non-preferred orientations. Indicating that the sharpening of orientation selectivity through recurrent inhibitory connectivity might also be a valid mechanism for the sharpening of extra-classical spike features such as endstopping.

Recurrent inhibitory connections between PV cells and pyramidal cells also have been linked to the maintenance of an excitation balance, preventing excessive excitatory activity that might otherwise lead to neural saturation or increased

noise (Ma et al., 2021). By selectively inhibiting pyramidal neurons that share similar visual selectivities and provide strong excitatory feedback, PV interneurons suppress potential excitatory overshoots. The optimal ratio of 1:10 PV interneurons to simple cells found in figure 11 fits the observation that PV cells make up 10% to 15% of cells in mouse V1 (Meyer et al., 2011). Moreover, figure 9a showed that PV activity can be used to gradually decrease endstopping behaviour even in the case that orientation deviate from their preferred orientation. In our model the inhibitory end zone had the same orientation preference as the excitatory component of the endstopped cell, however in physiology the PV cells could also receive activity related to other visual features.

In addition to local inhibitory recurrent connections in V1, there are also excitatory recurrent connections found between area LM and V1 (Muir et al., 2017). Their study explored how local excitatory connections in mouse V1 are not just simple like-to-like mappings but engage in complex feature-binding responses to visual stimuli. Specifically, they examined responses to plaid stimuli, which consist of overlapping grating patterns, to test different connectivity models. By comparing computational models with *in vivo* recordings, they discovered that the responses to plaid stimuli were better explained by a feature-binding connectivity scheme rather than simple like-to-like connectivity. This scheme suggests that local recurrent circuits in V1 selectively group neurons with differing visual properties to form excitatory subnetworks. These subnetworks dynamically amplify and integrate multiple feedforward inputs, allowing for more complex and selective visual processing than would be possible with simple like-to-like

connections. This feature-binding mechanism allows V1 to generate facilitatory responses to plaid stimuli that are not predictable from responses to individual grating components, highlighting the role of local recurrent circuitry in shaping perceptual outputs based on composite visual inputs.

Furthermore, in work by Marques et al. (2018), they observed that feedback connections from LM to V1 preferentially targeted retinotopically matching location, however that orientation selective axons spread around the location perpendicularly to their preferred orientation. These findings are in line with predictions from the current model that highlights how direct feedback from LM to V1 could induce a perpendicular illusory contour if there is sufficient local recurrent activity. Complementing this, the study by Shin et al. (2023) demonstrated the functional significance of these recurrent pathways in the processing of illusory contours within V1. Their experimental evidence showed that V1 neurons recurrently amplify the activity to represent illusory contours, recreating V1 activity in the absence of explicit external cues. Thereby highlighting the essential role of recurrent connectivity in supporting sensory illusions and perceptual consistency of occluded figures. Feedback would in this case be orientation specific, however it might be physiologically beneficial for feedback projections to be broadly tuned to allow for the curved interpolation between points. By doing so, recurrent excitation could be leveraged to amplify the interactions between overlapping orientations, thereby enriching the model's ability to generate and interpolate complex visual structures. This feedback mechanism would allow for the formation of curved surfaces and the interpolation between non-orthogonal

points, capabilities that are currently absent in our model but are crucial for simulating a more realistic and robust visual perception process. This approach not only aligns with the physiological evidence suggesting that the visual cortex utilises broad, integrative feedback mechanisms to refine perceptual outputs but also opens new avenues for modelling how the brain interprets and reconstructs complex visual scenes from sparse inputs. By enabling the model to interpolate illusory contours more effectively, we anticipate a significant improvement in its ability to reconstruct detailed and continuous visual experiences from fragmented or partially occluded stimuli.

One limitation of the current models is that the tuning was done by hand. This made it difficult to tune the recurrent connections and feedback mechanisms. Future research should utilise deep learning strategies to automate weight tuning using large datasets. This way research can explore creative solutions that would be impossible to create by hand. At the heart of the current models lies the concept of recurrent endstopping, this structure can be specified as an initial condition for the algorithms to lead into a particular direction, with early layers capturing basic features like edges and orientations and endstopping. By specifying early layer structures we can provide a foundational framework for the network to reconstruct inducer shapes and represent illusory contours in a way that is still biologically plausible. Moreover, the tuning of the network's weights based on a substantial volume of input data allows the model to learn the complicated patterns and relationships that define illusory contours. This aspect of deep learning is pivotal because it embodies the principle of experience-driven plasticity seen

in biological systems, where exposure to a range of visual environments fine-tunes the perceptual capabilities of the system. The iterative process of weight adjustment and optimisation through techniques such as gradient descent enables the model to progressively enhance its accuracy and efficiency in predicting illusory contours.

## References

- Ashbridge, E., Perrett, D., Oram, M., & Jellema, T. (2000). Effect of Image Orientation and Size on Object Recognition: Responses of Single Units in the Macaque Monkey Temporal Cortex. *Cognitive Neuropsychology*, 17(1-3), 13–34. <https://doi.org/10.1080/026432900380463>
- Billeh, Y. N., Cai, B., Gratiy, S. L., Dai, K., Iyer, R., Gouwens, N. W., Abbasi-Asl, R., Jia, X., Siegle, J. H., Olsen, S. R., Koch, C., Mihalas, S., & Arkhipov, A. (2020). Systematic Integration of Structural and Functional Data into Multi-scale Models of Mouse Primary Visual Cortex. *Neuron*, 106(3), 388–403.e18. <https://doi.org/10.1016/j.neuron.2020.01.040>
- De Weerd, P., Desimone, R., & Ungerleider, L. G. (1996). Cue-dependent deficits in grating orientation discrimination after V4 lesions in macaques. *Visual Neuroscience*, 13(3), 529–538. <https://doi.org/10.1017/S0952523800008208>
- DeAngelis, G. C., Freeman, R. D., & Ohzawa, I. (1994). Length and width tuning of neurons in the cat's primary visual cortex. *Journal of Neurophysiology*, 71(1), 347–374. <https://doi.org/10.1152/jn.1994.71.1.347>
- Durand, S., Iyer, R., Mizuseki, K., de Vries, S., Mihalas, S., & Reid, R. C. (2016). A Comparison of Visual Response Properties in the Lateral Geniculate Nucleus and Primary Visual Cortex of Awake and Anesthetized Mice. *Journal of Neuroscience*, 36(48), 12144–12156. <https://doi.org/10.1523/JNEUROSCI.1741-16.2016>

- Fan, J., & Zeng, Y. (2023). Challenging deep learning models with image distortion based on the abutting grating illusion. *Patterns (New York, N.Y.)*, 4(3), 100695. <https://doi.org/10.1016/j.patter.2023.100695>
- Felleman, D. J., & Van Essen, D. C. (1991). Distributed hierarchical processing in the primate cerebral cortex. *Cerebral Cortex (New York, N.Y.: 1991)*, 1(1), 1–47. <https://doi.org/10.1093/cercor/1.1.1-a>
- Ferster, D., Chung, S., & Wheat, H. (1996). Orientation selectivity of thalamic input to simple cells of cat visual cortex. *Nature*, 380(6571), 249–252. <https://doi.org/10.1038/380249a0>
- Gămănuț, R., & Shimaoka, D. (2022). Anatomical and functional connectomes underlying hierarchical visual processing in mouse visual system. *Brain Structure and Function*, 227(4), 1297–1315. <https://doi.org/10.1007/s00429-021-02415-4>
- Grossberg, S., & Mingolla, E. (1987). The Role of Illusory Contours in Visual Segmentation. In S. Petry & G. E. Meyer (Eds.), *The Perception of Illusory Contours* (pp. 116–125). Springer. [https://doi.org/10.1007/978-1-4612-4760-9\\_12](https://doi.org/10.1007/978-1-4612-4760-9_12)
- Hooser, S. D. V., Heimel, J. A. F., Chung, S., Nelson, S. B., & Toth, L. J. (2005). Orientation Selectivity without Orientation Maps in Visual Cortex of a Highly Visual Mammal. *Journal of Neuroscience*, 25(1), 19–28. <https://doi.org/10.1523/JNEUROSCI.4042-04.2005>
- Hubel, D. H., & Wiesel, T. N. (1962). Receptive fields, binocular interaction and functional architecture in the cat's visual cortex. *The Journal of*

- Physiology*, 160(1), 106–154. <https://doi.org/10.1113/jphysiol.1962.sp006837>
- Hubel, D. H., & Wiesel, T. N. (1965). RECEPTIVE FIELDS AND FUNCTIONAL ARCHITECTURE IN TWO NONSTRIATE VISUAL AREAS (18 AND 19) OF THE CAT. *Journal of Neurophysiology*, 28(2), 229–289. <https://doi.org/10.1152/jn.1965.28.2.229>
- Jones, H. E., Grieve, K. L., Wang, W., & Sillito, A. M. (2001). Surround Suppression in Primate V1. *Journal of Neurophysiology*, 86(4), 2011–2028. <https://doi.org/10.1152/jn.2001.86.4.2011>
- Kanizsa, G. (1976). Subjective Contours. *Scientific American*, 234(4), 48–53.
- Kirchberger, L., Mukherjee, S., Schnabel, U. H., van Beest, E. H., Barsegian, A., Levelt, C. N., Heimel, J. A., Lorteije, J. A. M., van der Togt, C., Self, M. W., & Roelfsema, P. R. (2020). The essential role of feedback processing for figure-ground perception in mice. <https://doi.org/10.1101/456459>
- Lee, T. S., & Nguyen, M. (2001). Dynamics of subjective contour formation in the early visual cortex. *Proceedings of the National Academy of Sciences*, 98(4), 1907–1911. <https://doi.org/10.1073/pnas.98.4.1907>
- Li, Y.-t., Ma, W.-p., Li, L.-y., Ibrahim, L. A., Wang, S.-z., & Tao, H. W. (2012). Broadening of Inhibitory Tuning Underlies Contrast-Dependent Sharpening of Orientation Selectivity in Mouse Visual Cortex. *Journal of Neuroscience*, 32(46), 16466–16477. <https://doi.org/10.1523/JNEUROSCI.3221-12.2012>

- Luongo, F. J., Liu, L., Ho, C. L. A., Hesse, J. K., Wekselblatt, J. B., Lanfranchi, F. F., Huber, D., & Tsao, D. Y. (2023). Mice and primates use distinct strategies for visual segmentation (M. Vinck, J. I. Gold, & M. W. Self, Eds.). *eLife*, 12, e74394. <https://doi.org/10.7554/eLife.74394>
- Ma, G., Liu, Y., Wang, L., Xiao, Z., Song, K., Wang, Y., Peng, W., Liu, X., Wang, Z., Jin, S., Tao, Z., Li, C. T., Xu, T., Xu, F., Xu, M., & Zhang, S. (2021). Hierarchy in sensory processing reflected by innervation balance on cortical interneurons. *Science Advances*, 7(20), eabf5676. <https://doi.org/10.1126/sciadv.abf5676>
- Markov, N. T., Vezoli, J., Chameau, P., Falchier, A., Quilodran, R., Huissoud, C., Lamy, C., Misery, P., Giroud, P., Ullman, S., Barone, P., Dehay, C., Knoblauch, K., & Kennedy, H. (2014). Anatomy of hierarchy: Feed-forward and feedback pathways in macaque visual cortex. *Journal of Comparative Neurology*, 522(1), 225–259. <https://doi.org/10.1002/cne.23458>
- Marques, T., Nguyen, J., Fioreze, G., & Petreanu, L. (2018). The functional organization of cortical feedback inputs to primary visual cortex. *Nature Neuroscience*, 21(5), 757–764. <https://doi.org/10.1038/s41593-018-0135-z>
- Martinez, L. M., Wang, Q., Reid, R. C., Pillai, C., Alonso, J.-M., Sommer, F. T., & Hirsch, J. A. (2005). Receptive field structure varies with layer in the primary visual cortex. *Nature Neuroscience*, 8(3), 372–379. <https://doi.org/10.1038/nn1404>

- Mechler, F., & Ringach, D. L. (2002). On the classification of simple and complex cells. *Vision Research*, 42(8), 1017–1033. [https://doi.org/10.1016/S0042-6989\(02\)00025-1](https://doi.org/10.1016/S0042-6989(02)00025-1)
- Mendola, J. D., Dale, A. M., Fischl, B., Liu, A. K., & Tootell, R. B. H. (1999). The Representation of Illusory and Real Contours in Human Cortical Visual Areas Revealed by Functional Magnetic Resonance Imaging. *The Journal of Neuroscience*, 19(19), 8560–8572. <https://doi.org/10.1523/JNEUROSCI.19-19-08560.1999>
- Meyer, H. S., Schwarz, D., Wimmer, V. C., Schmitt, A. C., Kerr, J. N., Sakmann, B., & Helmstaedter, M. (2011). Inhibitory interneurons in a cortical column form hot zones of inhibition in layers 2 and 5A. *Proceedings of the National Academy of Sciences*, 108(40), 16807–16812.
- Moskovitz, T. H., Roy, N. A., & Pillow, J. W. (2018). A comparison of deep learning and linear-nonlinear cascade approaches to neural encoding. <https://doi.org/10.1101/463422>
- Muir, D. R., Molina-Luna, P., Roth, M. M., Helmchen, F., & Kampa, B. M. (2017). Specific excitatory connectivity for feature integration in mouse primary visual cortex. *PLoS Computational Biology*, 13(12), e1005888. <https://doi.org/10.1371/journal.pcbi.1005888>
- Nguyen, G., & Freeman, A. W. (2019). A model for the origin and development of visual orientation selectivity. *PLOS Computational Biology*, 15(7), e1007254. <https://doi.org/10.1371/journal.pcbi.1007254>

- Niell, C. M., & Scanziani, M. (2021). How Cortical Circuits Implement Cortical Computations: Mouse Visual Cortex as a Model. *Annual Review of Neuroscience*, 44(Volume 44, 2021), 517–546. <https://doi.org/10.1146/annurev-neuro-102320-085825>
- Niell, C. M., & Stryker, M. P. (2008). Highly selective receptive fields in mouse visual cortex. *The Journal of Neuroscience: The Official Journal of the Society for Neuroscience*, 28(30), 7520–7536. <https://doi.org/10.1523/JNEUROSCI.0623-08.2008>
- Orban, G. A., Kato, H., & Bishop, P. O. (1979). Dimensions and properties of end-zone inhibitory areas in receptive fields of hypercomplex cells in cat striate cortex. *Journal of Neurophysiology*, 42(3), 833–849. <https://doi.org/10.1152/jn.1979.42.3.833>
- Pak, A., Ryu, E., Li, C., & Chubykin, A. A. (2020). Top-Down Feedback Controls the Cortical Representation of Illusory Contours in Mouse Primary Visual Cortex. *The Journal of Neuroscience*, 40(3), 648–660. <https://doi.org/10.1523/JNEUROSCI.1998-19.2019>
- Palmer, S. E., & Nelson, R. (2000). Late influences on perceptual grouping: Illusory figures. *Perception & Psychophysics*, 62(7), 1321–1331. <https://doi.org/10.3758/BF03212134>
- Pan, Y., Chen, M., Yin, J., An, X., Zhang, X., Lu, Y., Gong, H., Li, W., & Wang, W. (2012). Equivalent Representation of Real and Illusory Contours in Macaque V4. *Journal of Neuroscience*, 32(20), 6760–6770. <https://doi.org/10.1523/JNEUROSCI.6140-11.2012>

- Rockland, K. S. (2019). What do we know about laminar connectivity? *NeuroImage*, 197, 772–784. <https://doi.org/10.1016/j.neuroimage.2017.07.032>
- Roelfsema, P. R. (2006). CORTICAL ALGORITHMS FOR PERCEPTUAL GROUPING. *Annual Review of Neuroscience*, 29(1), 203–227. <https://doi.org/10.1146/annurev.neuro.29.051605.112939>
- Sceniak, M. P., Hawken, M. J., & Shapley, R. (2001). Visual Spatial Characterization of Macaque V1 Neurons. *Journal of Neurophysiology*, 85(5), 1873–1887. <https://doi.org/10.1152/jn.2001.85.5.1873>
- Schnabel, U. H., Bossens, C., Lorteije, J. A. M., Self, M. W., Op De Beeck, H., & Roelfsema, P. R. (2018). Figure-ground perception in the awake mouse and neuronal activity elicited by figure-ground stimuli in primary visual cortex. *Scientific Reports*, 8(1), 17800. <https://doi.org/10.1038/s41598-018-36087-8>
- Shin, H., Ogando, M. B., Abdeladim, L., Durand, S., Belski, H., Cabasco, H., Loefler, H., Bawany, A., Hardcastle, B., Wilkes, J., Nguyen, K., Suarez, L., Johnson, T., Han, W., Ouellette, B., Grasso, C., Swapp, J., Ha, V., Young, A., ... Adesnik, H. (2023). Recurrent pattern completion drives the neocortical representation of sensory inference. <https://doi.org/10.1101/2023.06.05.543698>
- Shushruth, S., Mangapathy, P., Ichida, J. M., Bressloff, P. C., Schwabe, L., & Angelucci, A. (2012). Strong Recurrent Networks Compute the Orientation Tuning of Surround Modulation in the Primate Primary Visual Cortex.

- Journal of Neuroscience*, 32(1), 308–321. <https://doi.org/10.1523/JNEUROSCI.3789-11.2012>
- Sillito, A. M., & Versiani, V. (1977). The contribution of excitatory and inhibitory inputs to the length preference of hypercomplex cells in layers II and III of the cat's striate cortex. *The Journal of Physiology*, 273(3), 775–790.
- Skottun, B. C., De Valois, R. L., Grosof, D. H., Movshon, J. A., Albrecht, D. G., & Bonds, A. (1991). Classifying simple and complex cells on the basis of response modulation. *Vision Research*, 31(7-8), 1078–1086. [https://doi.org/10.1016/0042-6989\(91\)90033-2](https://doi.org/10.1016/0042-6989(91)90033-2)
- Soriano, M., Spillmann, L., & Bach, M. (1996). The abutting grating illusion. *Vision Research*, 36(1), 109–116. [https://doi.org/10.1016/0042-6989\(95\)00107-b](https://doi.org/10.1016/0042-6989(95)00107-b)
- Van Rossum, G., & Drake Jr, F. L. (1995). *Python tutorial* (Vol. 620). Centrum voor Wiskunde en Informatica Amsterdam, The Netherlands.
- Von Der Heydt, R., & Peterhans, E. (1989). Mechanisms of contour perception in monkey visual cortex. I. Lines of pattern discontinuity. *The Journal of Neuroscience*, 9(5), 1731–1748. <https://doi.org/10.1523/JNEUROSCI.09-05-01731.1989>
- Von Der Heydt, R., Peterhans, E., & Baumgartner, G. (1984). Illusory Contours and Cortical Neuron Responses. *Science*, 224(4654), 1260–1262. <https://doi.org/10.1126/science.6539501>

- Wang, Q., & Burkhalter, A. (2007). Area map of mouse visual cortex. *Journal of Comparative Neurology*, 502(3), 339–357. <https://doi.org/10.1002/cne.21286>
- Wilson, H. R., & Cowan, J. D. (1972). Excitatory and Inhibitory Interactions in Localized Populations of Model Neurons. *Biophysical Journal*, 12(1), 1–24. [https://doi.org/10.1016/S0006-3495\(72\)86068-5](https://doi.org/10.1016/S0006-3495(72)86068-5)
- Wyatte, D., Jilk, D. J., & O'Reilly, R. C. (2014). Early recurrent feedback facilitates visual object recognition under challenging conditions. *Frontiers in Psychology*, 5. <https://doi.org/10.3389/fpsyg.2014.00674>
- Znamenskiy, P., Kim, M.-H., Muir, D. R., Iacaruso, M. F., Hofer, S. B., & Mrsic-Flogel, T. D. (2024). Functional specificity of recurrent inhibition in visual cortex. *Neuron*, 112(6), 991–1000.e8. <https://doi.org/10.1016/j.neuron.2023.12.013>